

Wideband Relative Transfer Function (RTF) Estimation Exploiting Frequency Correlations

Giovanni Bologni, Richard C. Hendriks and Richard Heusdens

Abstract—This article focuses on estimating relative transfer functions (RTFs) for beamforming applications. While traditional methods assume that spectra are uncorrelated, this assumption is often violated in practical scenarios due to natural phenomena such as the Doppler effect, artificial manipulations like time-domain windowing, or the non-stationary nature of the signals, as observed in speech. To address this, we propose an RTF estimation technique that leverages spectral and spatial correlations through subspace analysis. To overcome the challenge of estimating second-order spectral statistics for real data, we employ a phase-adjusted estimator originally proposed in the context of engine fault detection. Additionally, we derive Cramér–Rao bounds (CRBs) for the RTF estimation task, providing theoretical insights into the achievable estimation accuracy. The bounds show that channel estimation can be performed more accurately if the noise or the target presents spectral correlations. Experiments on real and synthetic data show that our technique outperforms the narrowband maximum-likelihood estimator when the target exhibits spectral correlations. Although the accuracy of the proposed algorithm is generally close to the bound, there is some room for improvement, especially when noise signals with high spectral correlation are present. While the applications of channel estimation are diverse, we demonstrate the method in the context of array processing for speech.

Index Terms—Acoustic parameter estimation, relative transfer function, RTF, Cramér–Rao bound, CRB, correlation, channel.

I. INTRODUCTION

SPATIAL filtering techniques can extract a target signal from the measurements of multiple sensors, also referred to as *beamforming* [1], [2]. Most beamforming techniques, such as the minimum variance distortionless beamformer (MVDR) and the multi-channel Wiener filter (MWF), rely on the knowledge of the relative transfer function (RTF) between a target emitter and a sensor array to virtually *steer* the array towards the direction of interest [3], [4]. RTFs generalize the angle or direction-of-arrival (DOA) concept in scenarios involving the proximity of the source to the receivers or the presence of reflections. These scenarios commonly arise in acoustics and wireless communications, radar and sonar sensing, seismology, and medical imaging.

One fundamental assumption shared among many channel estimation techniques is that RTFs can be estimated independently per frequency bin after transforming the received signal to the short-time Fourier transform (STFT) domain [5]–[11]. This implies that the signals are realizations of wide-sense stationary (WSS) processes or that distinct frequency components of the signal are mutually uncorrelated. It was shown that distinct frequency components of a random process are statistically uncorrelated if and only if the process is WSS [12].

However, the spectral uncorrelation assumption is frequently violated in practice. The STFT coefficients of the signals in

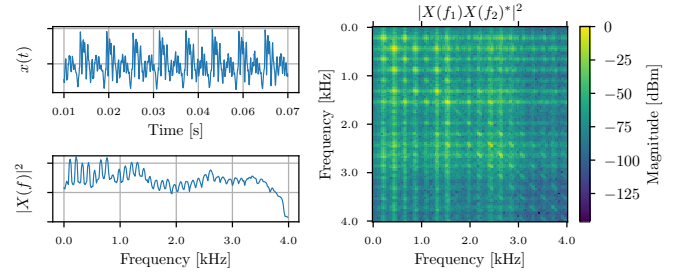


Fig. 1. The /a/ phoneme uttered by a male speaker. The top left plot depicts the waveform, while the bottom left plot shows the power spectral density (PSD). The peaks in the PSD are found at integer multiples of the fundamental frequency (harmonics). The right plot shows the spectral correlation or bifrequency spectrum. The grid-like structure of peaks in the bifrequency spectrum, whose spacing is proportional to the fundamental frequency, indicates a correlation between harmonic components [13].

neighboring frequency bands are correlated due to the use of short frame lengths and overlap-add/save techniques. In wireless communications, non-stationarity might be due to natural phenomena like the Doppler effect or artificial manipulations such as in orthogonal frequency division multiplexing (OFDM) [13], [14]. In the audio processing domain, vowels are often modeled as an impulse train filtered by a time-varying linear filter. Figure 1 shows the waveform $x(t)$ of the /a/ phoneme uttered by a male speaker, its power spectral density (PSD), and its bifrequency spectrum. The bifrequency spectrum approximates $\mathbb{E}[X(f_1)X(f_2)^*]$ for all frequencies f_1, f_2 , where $\mathbb{E}[\cdot]$ indicates the expected value and $X(f)$ is the Fourier transform of $x(t)$. The vowel in Figure 1 has a non-diagonal bifrequency spectrum, implying that its frequency components are correlated. First of all, this is not in line with the typical assumptions being made: estimation of parameters or processes from such an acoustic scene could be impaired. Secondly, we can conclude that $x(t)$ cannot be modeled as a realization of a WSS process, and the ergodicity assumption does not hold [15], [16].

Characterizing the spectral covariance of such a process requires a phase-adjusted estimator, whose details are discussed in this contribution as well.

Empirical studies on human auditory perception consistently highlight the practical importance of spectral correlations in spatial filtering. These correlations are critical in tasks such as sound localization and speech intelligibility. For instance, speech intelligibility in noise is influenced by the periodic structure of signals, with harmonically complex tones allowing for easier detection compared to inharmonic noise [17]. Additionally, humans can localize speakers based on spatially aliased measurements, but only when spectrally complex sounds are present [18], [19]. Dmochowsky *et al.* proved that spatial aliasing, a common issue in narrowband signals [20], has

reduced impact when the signals are wideband, regardless of the spatial sampling period [21]. Despite the compelling evidence of the relevance of wideband patterns, traditional channel estimation algorithms have rarely considered them explicitly.

Therefore, this paper aims to investigate the impact of spectral correlations on the channel estimation task. Our contributions are twofold: Firstly, we propose an RTF estimation technique based on subspace analysis that exploits spectral and spatial correlations. This technique consistently outperforms the narrowband maximum-likelihood estimator (MLE), known as covariance whitening (CW) [22]–[24], when the target exhibits spectral correlations. Secondly, we derive conditional and unconditional CRBs for the RTF estimation task. To the best of our knowledge, bounds for the RTF estimation task have not been derived before, not even for the narrowband scenario. The bounds show that channel estimation can be conducted more accurately if the target or the additive noise presents inter-frequency correlations. Our findings align with experiments showing that both parametric methods and methods based on deep neural network (DNN) for speech enhancement, which jointly process spectral information, outperform their counterparts that process each frequency bin independently [25]–[28]. Although the accuracy of the proposed algorithm is generally close to the bound, there is some room for improvement, especially when noise signals with high spectral correlation are present.

The article details the signal model in Section II. In Section III, we demonstrate how to recover the spectral-spatial covariance matrix of the source at the receivers. Based on these results, we propose a novel algorithm for RTF estimation in Section IV. To better assess the algorithms' performance, we compare them to the lower bounds on the variance of RTF estimation, which are derived in Section V. Numerical evidence of the superiority of the proposed algorithm, especially when the target presents spectral correlation, is provided in Section VI. In Section VII, we present additional discussion and insights on the experiments. Finally, some conclusions are drawn in Section VIII, summarizing the essential findings and contributions of this paper.

II. SIGNAL MODEL

In a reverberant and noisy environment, we consider the case of a single point source impinging on an array of $M \geq 2$ sensors. The signal received by the array is given in the STFT domain as:

$$\mathbf{x}_k(l) = \mathbf{d}_k(l) + \mathbf{v}_k(l) = s_k(l)\mathbf{a}_k + \mathbf{v}_k(l) \in \mathbb{C}^M, \quad (1)$$

where $\mathbf{d}_k(l) = s_k(l)\mathbf{a}_k$ is the target signal at the receiver, $l = 1, \dots, L$ is the time-frame index and the subscript $k = 1, \dots, K$ denotes the frequency bin index. The STFT coefficients of the target signal at the source are modeled by $s_k(l)$, which are realizations of complex random variables with zero mean. The target coefficients are *not* assumed to be mutually independent over frequency. They can follow any probability distribution. The transfer function $\mathbf{a}_k \in \mathbb{C}^M$ models the wave propagation from the target point source to the M different sensors. The transfer function is assumed to be

an unknown deterministic quantity that typically needs to be estimated in beamforming applications. The noise coefficients $\mathbf{v}_k(l)$ are also modeled as complex random variables with zero mean and an arbitrary probability distribution.

Let us now consider the coefficients for all frequency components jointly.

Noisy coefficients corresponding to a single time frame l , for M sensors, at K frequencies, can be stacked in a column vector as in

$$\mathbf{x} = [\mathbf{x}_1^T, \mathbf{x}_2^T, \dots, \mathbf{x}_K^T]^T \in \mathbb{C}^{KM}.$$

The time-frame index l is left out for notational convenience. In a similar fashion, noise vectors \mathbf{v}_k , transfer function vectors \mathbf{a}_k and desired signal \mathbf{d}_k can be stacked vertically to form \mathbf{v} , \mathbf{a} , and \mathbf{d} , respectively, so that $\mathbf{x} = \mathbf{d} + \mathbf{v}$. In this case, it is helpful to collect the signal coefficients s_k in a random vector $\bar{\mathbf{s}} = [s_1, s_2, \dots, s_K]^T$. Let us also define $\mathbf{s} = \bar{\mathbf{s}} \otimes \mathbf{1}_M = [s_1 \mathbf{1}_M^T, s_2 \mathbf{1}_M^T, \dots, s_K \mathbf{1}_M^T]^T$, where \otimes is the Kronecker product and $\mathbf{1}_M$ is the M -dimensional all-ones vector. Next, let

$$\mathbf{A} = \text{diag}(\mathbf{a}) = \text{diag}(a_{11}, \dots, a_{1M}, a_{21}, \dots, a_{KM}), \quad (2)$$

contain the transfer functions for all frequencies and sensors. The vector of desired signals is then given by

$$\mathbf{d} = \mathbf{A}\mathbf{s} = \mathbf{A}(\bar{\mathbf{s}} \otimes \mathbf{1}_M), \quad (3)$$

such that the noisy coefficients for the wideband model can be written as

$$\mathbf{x} = \mathbf{d} + \mathbf{v} = \mathbf{A}\mathbf{s} + \mathbf{v}. \quad (4)$$

Next, we model the spatial and spectral correlations between the signals. Spatial correlation matrices are widely used in array processing to model relations between signals received at different sensors. Here, we also consider *spectral* correlations between different frequency components.

The spectral-spatial covariance matrix $\mathbf{R}_x = \mathbb{E}[\mathbf{x}\mathbf{x}^H] \in \mathbb{C}^{KM \times KM}$, can be expressed as

$$\mathbf{R}_x = \begin{bmatrix} \mathbf{r}_x(1,1) & \mathbf{r}_x(1,2) & \cdots & \mathbf{r}_x(1,K) \\ \mathbf{r}_x(2,1) & \mathbf{r}_x(2,2) & \cdots & \\ \vdots & \vdots & \ddots & \vdots \\ \mathbf{r}_x(K,1) & \mathbf{r}_x(K,2) & \cdots & \mathbf{r}_x(K,K) \end{bmatrix}, \quad (5)$$

where $(\cdot)^H$ indicates the conjugate transpose operation, and $\mathbf{r}_x(i,j) = \mathbb{E}[\mathbf{x}_i \mathbf{x}_j^H] \in \mathbb{C}^{M \times M}$ is the bifrequency spatial covariance matrix at two arbitrary frequencies i, j . When noise and target signal are statistically uncorrelated, we have $\mathbf{R}_x = \mathbf{R}_d + \mathbf{R}_v$, that is,

$\mathbf{r}_x(i,j) = \mathbb{E}[s_i s_j^*] \mathbf{a}_i \mathbf{a}_j^H + \mathbb{E}[\mathbf{v}_i \mathbf{v}_j^H]$. Let us now introduce alternative formulations of the covariance matrices that will be useful for our analysis. Using the definition in Equation (3), the signal covariance matrix $\mathbf{R}_d = \mathbb{E}[\mathbf{d}\mathbf{d}^H]$ can be expressed as

$$\mathbf{R}_d = \mathbb{E}[\mathbf{A}\mathbf{s}\mathbf{s}^H\mathbf{A}^H] = \mathbf{A} \mathbb{E}[\mathbf{s}\mathbf{s}^H] \mathbf{A}^H = \mathbf{A}\mathbf{R}_s\mathbf{A}^H, \quad (6)$$

where \mathbf{R}_s is defined as $\mathbf{R}_s = \mathbb{E}[\mathbf{s}\mathbf{s}^H]$. Using the properties of the Kronecker product, the covariance matrix \mathbf{R}_s can, in turn, be rewritten as

$$\begin{aligned} \mathbf{R}_s &= \mathbb{E}[(\bar{\mathbf{s}} \otimes \mathbf{1}_M)(\bar{\mathbf{s}} \otimes \mathbf{1}_M)^H] = \mathbb{E}[\bar{\mathbf{s}}\bar{\mathbf{s}}^H \otimes \mathbf{1}_M \mathbf{1}_M^H] \\ &= \mathbb{E}[\bar{\mathbf{s}}\bar{\mathbf{s}}^H] \otimes \mathbf{1}_{M \times M} = \mathbf{R}_{\bar{\mathbf{s}}} \otimes \mathbf{1}_{M \times M}, \end{aligned} \quad (7)$$

where

$$\mathbf{R}_{\bar{\mathbf{s}}} = \mathbb{E}[\bar{\mathbf{s}}\bar{\mathbf{s}}^H] \in \mathbb{C}^{K \times K}. \quad (8)$$

III. ESTIMATION OF TARGET COVARIANCE MATRIX

This section begins by reporting a strategy to estimate sample spectral-spatial covariance matrices. It then demonstrates that the desired signal covariance matrix \mathbf{R}_d is singular, with its rank being limited by the number of frequency components K . Finally, it explores how the eigenvectors of \mathbf{R}_x and \mathbf{R}_d are affected by additive noise, and it reports a strategy for recovering \mathbf{R}_d .

A. Phase-adjusted sample covariance matrix

The commonly used sample covariance matrix estimate, serving as the MLE for jointly Gaussian WSS data, is expressed as

$$\tilde{\mathbf{R}}_x = \frac{1}{L} \sum_{l=1}^L \mathbf{x}(l)\mathbf{x}(l)^H, \quad (9)$$

where l is the realization index. Alternatively, l can be treated as a time-frame index assuming second-order ergodicity.

However, when spectral correlations are present, the WSS assumption becomes inaccurate, requiring an alternative estimator for the spectral-spatial covariance matrices. In the estimation of *spectral* correlations from STFT data, it is crucial to establish a connection among phase components across all frames and frequencies. Traditionally, phase components are linked to the beginning of each frame. Therefore, there is a need to connect these phase components to a common reference point, such as the signal's onset, as mentioned by Antoni [29]. The phase-adjusted noisy STFT data at frequency k is given by:

$$\mathbf{x}_k^c(l) = \mathbf{x}_k(l)e^{-j2\pi lRk/K}, \quad l = 1, \dots, L, \quad (10)$$

where R denotes the block shift between frames. The phase correction becomes superfluous when dealing with products of components at the same frequency, as the conjugation leads to the cancellation of the phase term: $\mathbf{x}_k^c(l)\mathbf{x}_k^c(l)^H = \mathbf{x}_k(l)\mathbf{x}_k(l)^H$. Similarly, the exponential term in Equation (10) is identically one, thus ineffective, when $R = K$, i.e., when adjacent frames do not overlap, or when independent realizations of the signals are used. Therefore, the correction of Equation (10) is applied solely in Section VI-C to the overlapping STFT frames of real speech signals before covariance matrix estimation, so that

$$\begin{aligned} \hat{r}_x(k_1, k_2) &= \frac{1}{L} \sum_{l=1}^L \mathbf{x}_{k_1}^c(l)\mathbf{x}_{k_2}^c(l)^H \\ &= \frac{1}{L} \sum_{l=1}^L \mathbf{x}_{k_1}(l)\mathbf{x}_{k_2}(l)^H e^{-j2\pi lR(k_1-k_2)/K}, \end{aligned} \quad (11)$$

for $k_1, k_2 = 1, \dots, K$.

B. Upper bound on the rank of target covariance matrix

Lemma 1 $\text{rank}(\mathbf{R}_d) \leq K$

Proof. To support this claim, we first state two well-known properties of the matrix rank. Consider two matrices $\mathbf{X} \in \mathbb{C}^{m \times n}$ and $\mathbf{Y} \in \mathbb{C}^{n \times p}$. According to [30], we have that:

$$\text{rank}(\mathbf{X}\mathbf{Y}) \leq \min(\text{rank}(\mathbf{X}), \text{rank}(\mathbf{Y})), \quad (12)$$

$$\text{rank}(\mathbf{X} \otimes \mathbf{Y}) = \text{rank}(\mathbf{X})\text{rank}(\mathbf{Y}). \quad (13)$$

The covariance matrix $\mathbf{R}_{\bar{s}} = \mathbb{E}[\bar{s}\bar{s}^H]$ in Equation (8) obeys $\text{rank}(\mathbf{R}_{\bar{s}}) \leq K$.

The rank of the all-one matrix, instead, is $\text{rank}(\mathbf{1}_{M \times M}) = 1$. From Equation (7) and the rank property of Kronecker products in Equation (13) it follows that

$$\text{rank}(\mathbf{R}_s) = \text{rank}(\mathbf{R}_{\bar{s}} \otimes \mathbf{1}_{M \times M}) = \text{rank}(\mathbf{R}_{\bar{s}}) \leq K. \quad (14)$$

It is now possible to analyze the matrix rank of \mathbf{R}_d :

$$\text{rank}(\mathbf{R}_d) = \text{rank}(\mathbf{A}\mathbf{R}_s\mathbf{A}^H) \quad (15)$$

$$\leq \min(\text{rank}(\mathbf{A}), \text{rank}(\mathbf{R}_s)) \quad (16)$$

$$= \min(KM, \text{rank}(\mathbf{R}_s)) \leq K, \quad (17)$$

where the inequality follows from the rank matrix product property in Equation (12) and Equation (14). This completes the proof. \square

C. Estimation of the target covariance matrix

Suppose that \mathbf{R}_x is known, and the noise exhibits uniform power across both space and frequency, remaining uncorrelated in both domains, i.e., $\mathbf{R}_v = V^2\mathbf{I}_{KM}$. As the identity matrix is diagonalizable by any unitary matrix,

$$\mathbf{R}_x = \mathbf{R}_d + V^2\mathbf{I} = \mathbf{V}\mathbf{\Lambda}\mathbf{V}^H + V^2\mathbf{I} = \mathbf{V}(\mathbf{\Lambda} + V^2\mathbf{I})\mathbf{V}^H.$$

Therefore, if the (phase-adjusted) sample covariance matrix $\hat{\mathbf{R}}_x = \hat{\mathbf{V}}\hat{\mathbf{\Lambda}}\hat{\mathbf{V}}^H$ has been estimated, the covariance matrix of the target at the sensors can be approximated by $\hat{\mathbf{R}}_d = \hat{\mathbf{V}} \max(\hat{\mathbf{\Lambda}} - \hat{\mathbf{V}}^2\mathbf{I}, 0)\hat{\mathbf{V}}^H$, where the $\max(\cdot, \cdot)$ operator forces the eigenvalues of the Hermitian positive semidefinite (HPSD) matrix $\hat{\mathbf{R}}_d$ to be non-negative.

If spatially or spectrally colored noise is present, the eigenvectors of \mathbf{R}_x and \mathbf{R}_d will differ. However, estimating $\hat{\mathbf{R}}_d$ and computing its eigenvalue decomposition is still possible if an estimate of the noise covariance matrix $\hat{\mathbf{R}}_v$ is available. The clean covariance matrix $\hat{\mathbf{R}}_d$ can be estimated from the generalized eigenvalue decomposition (GEVD) of $\hat{\mathbf{R}}_x$ and $\hat{\mathbf{R}}_v$ or from the eigenvalue decomposition of the prewhitened noisy covariance matrix $\hat{\mathbf{R}}_v^{-1/2}\hat{\mathbf{R}}_x\hat{\mathbf{R}}_v^{-1/2}$. The present examination will be limited to the GEVD because the two procedures are theoretically equivalent [31], [32]¹. Given the estimates $\hat{\mathbf{R}}_x$ and $\hat{\mathbf{R}}_v$, an estimate of the desired covariance matrix $\hat{\mathbf{R}}_d$ can be obtained as follows:

- 1) Computation of $\hat{\mathbf{R}}_x\mathbf{U} = \hat{\mathbf{R}}_v\mathbf{U}\mathbf{D}$ or, equivalently, $\mathbf{Q}^H\hat{\mathbf{R}}_x = \mathbf{D}\mathbf{Q}^H\hat{\mathbf{R}}_v$, where \mathbf{D} are the generalized eigenvalues, \mathbf{U} are the right generalized eigenvectors, \mathbf{Q} are the left generalized eigenvectors, and $\mathbf{U} = \mathbf{Q}^{-H}$.
- 2) Partitioning of the left eigenvectors $\mathbf{Q} = [\mathbf{Q}_x \ \mathbf{Q}_v]$, where \mathbf{Q}_x comprises of the first K columns of \mathbf{Q} .
- 3) Estimation of $\hat{\mathbf{R}}_d$ as $\hat{\mathbf{R}}_d = \mathbf{Q}_x \max(\mathbf{D}_x - \mathbf{I}, 0)\mathbf{Q}_x^H$,

where \mathbf{D}_x is a diagonal subblock comprising of the first K columns and rows of \mathbf{D} . Notice that in step 2), we keep the largest K eigenvalue-eigenvector pairs, as K is the maximum possible rank for $\hat{\mathbf{R}}_d$ (see Lemma 1).

¹A standard routine for computing the GEVD of HPSD matrices is based on Cholesky decomposition [30, Algorithm 8.7.1]. It is used in the popular LAPACK drivers [33] that are the backbone of Matlab and Numpy/Scipy.

IV. PROPOSED RTF ESTIMATION ALGORITHM: SVD-DIRECT

In the preceding sections, the investigation focused on the spectral-spatial covariance matrix of a noisy signal received from multiple sensors. The knowledge gained from this investigation can be applied to estimate the channel \mathbf{a} , provided that estimates of the spectral-spatial covariance for both the noisy signal $\hat{\mathbf{R}}_x$ and the noise-only signal $\hat{\mathbf{R}}_v$ are available. To this aim, we introduce a new method for RTF estimation. The proposed algorithm is based on a row partitioning of the estimated spectral-spatial covariance $\hat{\mathbf{R}}_d$, followed by an SVD on each frequency subblock. The approach is named **SVD-direct** to emphasize the simplicity of its implementation and the central role played by the singular value decomposition.

The basic idea of the proposed RTF estimation algorithm can be explained by an example. First, let us introduce a simplified case with $K = 2$ frequency components, to gain some intuition on the structure of $\mathbf{R}_d = \mathbf{A}\mathbf{R}_s\mathbf{A}^H$. We have that

$$\mathbf{R}_d = \begin{bmatrix} \mathbb{E}[|s_1|^2] \mathbf{a}_1 \mathbf{a}_1^H & \mathbb{E}[s_1 s_2^*] \mathbf{a}_1 \mathbf{a}_2^H \\ \mathbb{E}[s_2 s_1^*] \mathbf{a}_2 \mathbf{a}_1^H & \mathbb{E}[|s_2|^2] \mathbf{a}_2 \mathbf{a}_2^H \end{bmatrix} = \quad (18)$$

$$= \begin{bmatrix} \sigma_1^2 \mathbf{a}_1 \mathbf{a}_1^H & \sigma_{12} \mathbf{a}_1 \mathbf{a}_2^H \\ \sigma_{12}^* \mathbf{a}_2 \mathbf{a}_1^H & \sigma_2^2 \mathbf{a}_2 \mathbf{a}_2^H \end{bmatrix} = \begin{bmatrix} \mathbf{R}_d^{(1)} \\ \mathbf{R}_d^{(2)} \end{bmatrix}, \quad (19)$$

where we have introduced the auxiliary variables

$$\sigma_1^2 = \mathbb{E}[|s_1|^2], \quad \sigma_2^2 = \mathbb{E}[|s_2|^2], \quad \sigma_{12} = \mathbb{E}[s_1 s_2^*]$$

to simplify the notation. The transfer function for the i th frequency is $\mathbf{a}_i \in \mathbb{C}^M$. We also defined the block-matrices $\mathbf{R}_d^{(1)}, \mathbf{R}_d^{(2)} \in \mathbb{C}^{M \times 2M}$. The absence of spectral correlations in the source signal \mathbf{s} would lead to $\mathbb{E}[s_1 s_2^*] = \mathbb{E}[s_2 s_1^*] = 0$. Now, consider the block matrix $\mathbf{R}_d^{(1)} = [\sigma_1^2 \mathbf{a}_1 \mathbf{a}_1^H \quad \sigma_{12} \mathbf{a}_1 \mathbf{a}_2^H]$ in Equation (19). Notice that $\mathbf{R}_d^{(1)}$ is a rank-1 matrix, whose left principal singular vector is \mathbf{a}_1 . The right principal singular vector of $\mathbf{R}_d^{(1)}$ is proportional to $[\mathbf{a}_1^T \quad \mathbf{a}_2^T]^T$. To see this, consider the matrix product

$$\mathbf{R}_d^{(1)} (\mathbf{R}_d^{(1)})^H = (\sigma_1^2 \|\mathbf{a}_1\|^2 + \sigma_{12}^2 \|\mathbf{a}_2\|^2) \mathbf{a}_1 \mathbf{a}_1^H \quad (20)$$

from which it follows that $\mathbf{R}_d^{(1)} (\mathbf{R}_d^{(1)})^H$ is a rank-1 matrix with principal eigenvector \mathbf{a}_1 ². It follows that by decomposing $\mathbf{R}_d^{(1)}$ with an SVD and selecting the principal left singular component, \mathbf{a}_1 can be recovered up to a scalar factor.

The procedure above can be repeated for each subblock $\mathbf{R}_d^{(k)}$, $k = 1, \dots, K$, leading to the proposed wideband channel estimation method, **SVD-direct** (Algorithm 1). The function `Normalize` is defined as `Normalize($\mathbf{a}^{(k)}$) = $\mathbf{a}^{(k)} / [\mathbf{a}^{(k)}]_r$` , and $[\mathbf{a}^{(k)}]_r$ is the entry corresponding to the r -th (reference) sensor.

V. CRAMÉR–RAO LOWER BOUND

Based on the spectral-spatial covariance matrix of the signal received at the multiple sensors, we derived an algorithm for RTF estimation, taking correlation across frequency into account. To determine how close this algorithm is to the optimal performance, we compare it to the CRB.

In the following, we first define the CRB and show how to derive it when estimating a deterministic function of

²Throughout the paper, $\|\cdot\|$ indicates the 2-norm.

Algorithm 1 SVD-direct

Input: $\hat{\mathbf{R}}_x, \hat{\mathbf{R}}_v, M, K$

Output: RTF estimates $\hat{\mathbf{a}}$

Estimate $\hat{\mathbf{R}}_d$ from the GEVD (Section III-C).

$$\hat{\mathbf{R}}_d \leftarrow \text{GEVD_routine}(\hat{\mathbf{R}}_x, \hat{\mathbf{R}}_v)$$

Partition in K “fat” $M \times KM$ blocks

$$[(\hat{\mathbf{R}}_d^{(1)})^T, (\hat{\mathbf{R}}_d^{(2)})^T, \dots, (\hat{\mathbf{R}}_d^{(K)})^T]^T \leftarrow \hat{\mathbf{R}}_d$$

Per each frequency

for $k = 1, \dots, K$ **do**

$$\mathbf{P}^{(k)} \mathbf{D}^{(k)} \mathbf{Q}^{(k)} \leftarrow \text{SVD}(\hat{\mathbf{R}}_d^{(k)})$$

Rescale left principal singular vectors

$$\hat{\mathbf{a}}^{(k)} \leftarrow \text{Normalize}(\mathbf{p}_1^{(k)}).$$

end for

an unknown parameter. The CRB is then calculated for two scenarios: (i) a setting where the target signal $\mathbf{s}(l)$ is deterministic and known (Section V-B), and (ii) a scenario where the target signal has a known covariance matrix \mathbf{R}_s , but the signal realizations are unknown (Section V-C). Note that the former bound will lead to an unrealistic lower bound, as in the current scenario, $\mathbf{s}(l)$ is never known. The latter bound is realistic as it only assumes that the first- and second-order statistics are known. The two settings are also known as the deterministic or conditional CRB, and stochastic or unconditional CRB, respectively [34]. Although the CRBs are derived for the wideband scenario, they encompass the bounds for narrowband RTF estimation as a specific case.

A. Problem formulation

Let us consider the case where the parameters $\boldsymbol{\theta}$ to be estimated are complex-valued, deterministic but unknown, and the observed data matrix is $\mathbf{X} = [\mathbf{x}(1) \dots \mathbf{x}(L)]$. The distribution of the observed data is $p(\mathbf{X}; \boldsymbol{\theta})$. The Fisher information matrix (FIM) is found as the negative expected Hessian of the log-likelihood function:

$$\mathbf{I}_\theta = -\mathbb{E}[\nabla_\theta \nabla_\theta^H \ln p(\mathbf{X}; \boldsymbol{\theta})] = -\mathbb{E}[\nabla_\theta^2 \ln p(\mathbf{X}; \boldsymbol{\theta})], \quad (21)$$

where the expectation is taken with respect to $p(\mathbf{X}; \boldsymbol{\theta})$. The gradient and the Hessian are defined as

$$[\nabla_\theta f]_i = \partial f / \partial \theta_i, \quad [\nabla_\theta^2 f]_{ij} = \partial^2 f / \partial \theta_i \partial \theta_j^*,$$

and the partial derivatives are Wirtinger derivatives [35]. The covariance matrix \mathbf{R}_θ of any unbiased estimator $\hat{\boldsymbol{\theta}}$ of $\boldsymbol{\theta}$ satisfies $\mathbf{R}_\theta \succeq \mathbf{I}_\theta^{-1}$ ³. When the quantity to estimate is given by a

³ $\mathbf{A} \succeq \mathbf{B}$ means $\mathbf{A} - \mathbf{B}$ is positive semidefinite with \mathbf{A} and \mathbf{B} being Hermitian

function $\gamma = \mathbf{g}(\boldsymbol{\theta})$ of some underlying parameter, the bound follows as [36]

$$\mathbf{R}_{\hat{\gamma}} \succeq (\nabla_{\boldsymbol{\theta}} \mathbf{g}) \mathbf{I}_{\boldsymbol{\theta}}^{-1} (\nabla_{\boldsymbol{\theta}}^H \mathbf{g}), \quad (22)$$

where $\mathbf{R}_{\hat{\gamma}}$ is the covariance matrix of the estimator $\hat{\gamma} = \mathbf{g}(\hat{\boldsymbol{\theta}})$.

In the present case, we define a function $\mathbf{g} : \mathbb{C}^{2KM} \mapsto \mathbb{C}^{KM}$ that transforms a transfer function to a *relative* transfer function. It is given by

$$\mathbf{g}(\boldsymbol{\theta}) = \mathbf{g}([\mathbf{a}^T \ \mathbf{a}^H]^T) = \mathbf{a}/\mathbf{a}_{\text{ref}}, \quad (23)$$

where the division is intended element-wise and

$$\mathbf{a}_{\text{ref}} = [a_{1r} \mathbf{1}_M^T, a_{2r} \mathbf{1}_M^T, \dots, a_{Kr} \mathbf{1}_M^T]^T,$$

is the vector with the responses of the r th (reference) sensor at all frequencies. Notice that $\mathbf{g}(\cdot)$ corresponds to the `Normalize`(\cdot) function defined in Section IV, with the only difference that $\mathbf{g}(\cdot)$ acts on transfer functions for all frequencies and sensors simultaneously. This function can be readily modified to accommodate various strategies for reference sensor selection [1, Eq. 10].

B. Conditional Cramér–Rao bound

Consider the model from Equation (4):

$$\mathbf{x}(l) = \mathbf{A} \mathbf{s}(l) + \mathbf{v}(l), \quad l = 1, \dots, L. \quad (24)$$

Firstly, we analyze the case where the signal $\mathbf{s}(l)$ is known and the absolute transfer function \mathbf{A} , defined in Equation (2), is deterministic but unknown. The noise $\mathbf{v}(l)$ is a complex circular Gaussian random process with known spectral-spatial covariance \mathbf{R}_v . The vector of unknown parameters is $\boldsymbol{\theta} = [\mathbf{a}^T \ \mathbf{a}^H]^T \in \mathbb{C}^{2KM}$. The observed data \mathbf{X} follows a complex Gaussian distribution so that the log-likelihood is given by

$$\ln p(\mathbf{X}; \boldsymbol{\theta}) = -L \ln |\pi \mathbf{R}_v| - \sum_{l=1}^L \mathbf{v}(l)^H \mathbf{R}_v^{-1} \mathbf{v}(l). \quad (25)$$

We have the following result.

Theorem 1 (Conditional CRB) *The variance of any conditional RTF estimator is lower bounded by:*

$$\text{CRB}[\mathbf{g}(\hat{\boldsymbol{\theta}})]_i = [(\nabla_{\mathbf{a}} \mathbf{g})(\mathbf{B}^*)^{-1} (\nabla_{\mathbf{a}}^H \mathbf{g})]_{ii}, \quad (26)$$

for $i = 1, \dots, M$, where the matrix \mathbf{B} is defined as $\mathbf{B} = \sum_{l=1}^L \mathbf{S}(l)^H \mathbf{R}_v^{-1} \mathbf{S}(l)$ and $\mathbf{S}(l) = \text{diag}(\mathbf{s}(l))$.

Proof. See Appendix A. \square

C. Unconditional Cramér–Rao bound

Consider again the model in Equation (24). This time, we examine the more realistic scenario where the spectral-spatial covariance of the target signal \mathbf{R}_s is known but not the signal itself. The transfer function \mathbf{A} is again deterministic but unknown. This bound is then expected to be greater than the one derived in Theorem 1 because the target signal is only known up to its second-order statistics. In this case, the log-likelihood function is given by:

$$\ln p(\mathbf{X}; \boldsymbol{\theta}) = -L \ln |\pi \hat{\mathbf{R}}_x| - L \text{tr}(\hat{\mathbf{R}}_x \mathbf{R}_x^{-1}), \quad (27)$$

where $\hat{\mathbf{R}}_x = \mathbf{A} \mathbf{R}_s \mathbf{A}^H + \mathbf{R}_v$. We have the following result.

Theorem 2 (Unconditional CRB) *In the unconditional settings, the variance of any unbiased RTF estimator is lower bounded by:*

$$\text{CRB}[\mathbf{g}(\hat{\boldsymbol{\theta}})]_i = [(\nabla_{\mathbf{a}} \mathbf{g}) \mathbf{C} (\nabla_{\mathbf{a}}^H \mathbf{g})]_{ii}, \quad (28)$$

for $i = 1, \dots, M$,

where \mathbf{C} is obtained by selecting the first KM rows and columns from the inverse FIM $\mathbf{I}_{\boldsymbol{\theta}}^{-1}$.

Proof. See Appendix B. \square

The CRB for proper complex-valued multivariate Gaussian parameters has been previously explored. In [37, Eq. 15.52], an approach that treats the real and imaginary components of the parameters independently was adopted. Conversely, in [38, Eq. 6.55], the Wirtinger derivatives were employed. However, neither of these references extends its analysis to incorporate further deterministic transformations.

VI. NUMERICAL SIMULATIONS

In the preceding sections, we developed an RTF estimation algorithm that considers both spectral and spatial correlations. We computed conditional and unconditional CRBs to gauge achievable accuracy. Following this, we conduct simulations to compare the performance of our proposed wideband algorithm (SVD-direct) to the benchmark narrowband method (CW) and the established performance bounds. We employ two error metrics, the root-mean-squared-error (RMSE) and the Hermitian angle [6]. The RMSE is defined as:

$$\text{RMSE} = 10 \log \sqrt{\frac{1}{KM} \|\hat{\mathbf{a}} - \mathbf{a}\|^2} \text{ (dB)}, \quad (29)$$

while the Hermitian angle is calculated as:

$$\frac{1}{K} \sum_{k=1}^K \text{acos} \left(\frac{|\hat{\mathbf{a}}_k^H \mathbf{a}_k|}{\|\hat{\mathbf{a}}_k^H\| \|\mathbf{a}_k\|} \right) \text{ (rad)}. \quad (30)$$

The RMSE accounts for discrepancies in the magnitude and phase, whereas the Hermitian angle depends exclusively on the angle between the RTFs, hence their phase differences. The CRBs are only defined for error measures based on the MSE. Therefore, these bounds are not shown in the plots that employ the Hermitian angle metric. We also define the signal-to-noise ratio (SNR) in the frequency domain as:

$$\text{SNR} = 10 \log \frac{\sum_{i=1}^{KM} [\mathbf{R}_d]_{ii}}{\sum_{i=1}^{KM} [\mathbf{R}_v]_{ii}} \text{ (dB)}. \quad (31)$$

In all plots, points connected by a continuous red line show the error for the proposed algorithm (Algorithm 1); points connected by a blue dotted line show errors for the benchmark algorithm (CW); points connected by a green dash-dotted line show the conditional CRB (Theorem 1); points connected by a purple dashed line show the unconditional CRB (Theorem 2).

Three sets of experiments are conducted to explore increasingly realistic scenarios. In the first two sets of experiments (Sections VI-A and VI-B), we analyze scenarios where independent realizations of the signals are drawn from ideal multivariate Gaussian distributions. In Section VI-A, the target

and noise powers at all frequencies are set to the same value and then rescaled to the desired SNR. Section VI-B describes a more realistic scenario where target and noise powers vary across frequencies. Results are shown for a single random draw of the target TF \mathbf{a} and of the actual covariance matrices \mathbf{R}_s and \mathbf{R}_v because the CRB is defined for specific parameter values. Nonetheless, similar outcomes are observed for other realizations. To simulate the complex channel vector \mathbf{a} , we generate two uniformly distributed random vectors with values from -1 to 1 and use them for the real and imaginary parts.

For the synthetic data of Sections VI-A and VI-B, the lines in the figures are the mean results averaged across 5000 Montecarlo realizations. The faded area represents the 95% confidence interval [39]. The bounds are evaluated at the actual values of the parameters. The third set of experiments of Section VI-C validates our approach by applying the algorithms to anechoic speech convolved with real room impulse responses (RIRs). In this case, the covariance matrices are estimated from overlapping STFT data. The ground truth TF \mathbf{a} is computed as the discrete Fourier transform of the first K samples of the RIR. We perform 50 Montecarlo repetitions of the real-data experiments.

Gaussian noise at 40 dB SNR is added to \mathbf{v} in all experiments to account for sensor noise and simultaneously improve numerical conditioning of the inverse of the noise covariance matrix \mathbf{R}_v . All the simulations are implemented in Python. In the spirit of reproducible research, the code to generate all figures in the paper is freely available online⁴.

A. Equicorrelated, equal powers

The ‘equicorrelated’ formulation, also considered in [40], assumes that the noise signal exhibits identical variances at all sensors and frequency components. The target signal has unit variance at all frequency components. The cross-expectations over different frequency components are v_f for the noise and ρ_f for the target. Because the frequency correlations are non-zero, the covariance matrices \mathbf{R}_x and \mathbf{R}_v describe non-WSS processes. Taking again the case of $M = 2$ sensors and $K = 2$ frequency components to simplify the exposition, the noise covariance matrix \mathbf{R}_v is given by:

$$\mathbf{R}_v = V^2 \begin{bmatrix} 1 & 0 & v_f & 0 \\ 0 & 1 & 0 & v_f \\ v_f^* & 0 & 1 & 0 \\ 0 & v_f^* & 0 & 1 \end{bmatrix}, \quad (32)$$

where $v_f \in [0, 1]$ and V^2 is scaled according to Equation (31) to yield the desired SNR.

Similarly, the desired covariance matrix at the source $\mathbf{R}_s = \mathbf{R}_s \otimes \mathbf{1}_{M \times M}$ is given by:

$$\mathbf{R}_s = \begin{bmatrix} 1 & \rho_f \\ \rho_f^* & 1 \end{bmatrix} \otimes \mathbf{1}_{M \times M} = \begin{bmatrix} 1 & 1 & \rho_f & \rho_f \\ 1 & 1 & \rho_f & \rho_f \\ \rho_f^* & \rho_f^* & 1 & 1 \\ \rho_f^* & \rho_f^* & 1 & 1 \end{bmatrix}. \quad (33)$$

The desired covariance matrix at the receivers follows from Equation (6). The stimuli $s(l)$ and $v(l)$, where l is the realization index, are generated through affine transformations

applied to L independent and identically distributed realizations $\mathbf{n}(l)$ of a white complex multivariate Gaussian distribution $\mathbf{n} \sim \mathcal{CN}(\mathbf{0}, \mathbf{I})$. For example, $s(l) = \mathbf{R}_s^{1/2} \mathbf{n}(l)$, and this implies $s(l) \sim \mathcal{CN}(\mathbf{0}, \mathbf{R}_s)$. The estimates of the target and noise covariance matrices are derived through the sample covariance estimator of Equation (9). The phase-corrected estimator in Equation (11) is indeed superfluous when independent signal realizations are available. Unless specified differently, the SNR is set to -5 dB in all experiments. The signal correlation is set to $\rho_f = 0.25$, the noise correlation to $v_f = 0.25$, the number of frames to compute the sample covariance matrices to $L = 1000$, the number of sensors to $M = 2$ and the FFT length to $K = 5$. The true noise covariance matrix \mathbf{R}_v is used in all algorithms, aligning with the CRB assumptions. Nonetheless, we noticed similar results when estimating \mathbf{R}_v from a separate realization of the noise-only signal. The algorithms and the bounds are tested by varying four independent parameters: noise correlation v_f , target correlation ρ_f , number of time frames L , and SNR.

Varying noise correlation v_f : In the first experiment, we analyze the performance of the algorithms as the noise frequency correlation v_f varies between 0 and 1 (Figure 2). We generally observe that the RMSE and the Hermitian angle metrics follow similar trends. Let us first consider the scenario where the target has low correlation ($\rho_f = 0.25$), corresponding to Figures 2a and 2b. The two algorithms perform equally well when the noise correlation v_f is low, while the proposed method shows improved accuracy for high values of v_f . In other words, the SVD-direct algorithm can partially take advantage of increased noise correlation, while the benchmark algorithm cannot. Now, consider the case where the target shows high correlation ($\rho_f = 0.75$), corresponding to Figures 2c and 2d. The proposed method outperforms the benchmark for all values of v_f , with improvements of approximately 3 dB in RMSE and 0.02 rad in Hermitian angle. Examining the conditional and unconditional CRBs, we note that substantial accuracy improvements are achievable when the noise exhibits a high correlation.

Varying target correlation ρ_f : In this section, we analyze the performance of the algorithms as the target frequency correlation ρ_f varies between 0 and 1 (Figure 3). Because SVD-direct is explicitly designed to take advantage of spectral correlations in the target, we expect it to yield better performance for higher values of ρ_f . If the noise has low correlation ($v_f = 0.25$, corresponding to the top row in Figure 3), the two algorithms perform equally well for low target correlation values ρ_f . Additionally, we observe that the proposed method can fully exploit the target correlation and shows improvements in the accuracy of up to 4 dB in RMSE and 0.02 rad in Hermitian angle for high values of ρ_f . The benchmark algorithm is not affected by variations in the target spectral correlation. Notice that the proposed algorithm achieves the CRB if a high target correlation is present, meaning that further improvements in accuracy in this scenario are not possible. Interestingly, the unconditional performance bound exhibits different trends for low and high noise correlation. The unconditional bound decreases with higher target correlations when the noise correlation is low (Figure 3a). Conversely, the maximum accuracy is lower as the target correlation increases for high noise correlation (Figure 3c). This aligns with findings

⁴<https://github.com/Screen/SVD-direct>

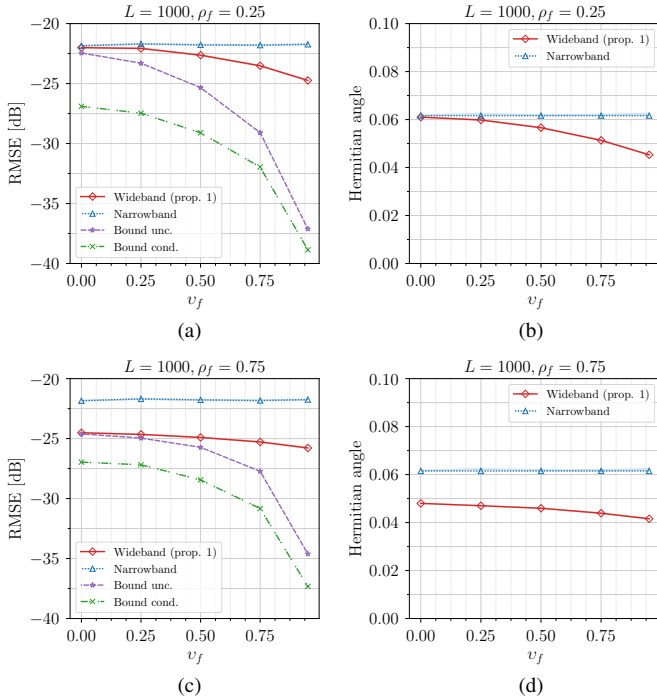


Fig. 2. Algorithm performance under varying noise frequency correlation v_f , with different levels of target correlation ρ_f . The top two plots (a) and (b) represent a less correlated target ($\rho_f = 0.25$), while the bottom row (c) and (d) show a highly correlated target ($\rho_f = 0.75$). Each column corresponds to different evaluation metrics: the left column displays the RMSE, and the right column shows the Hermitian angle.

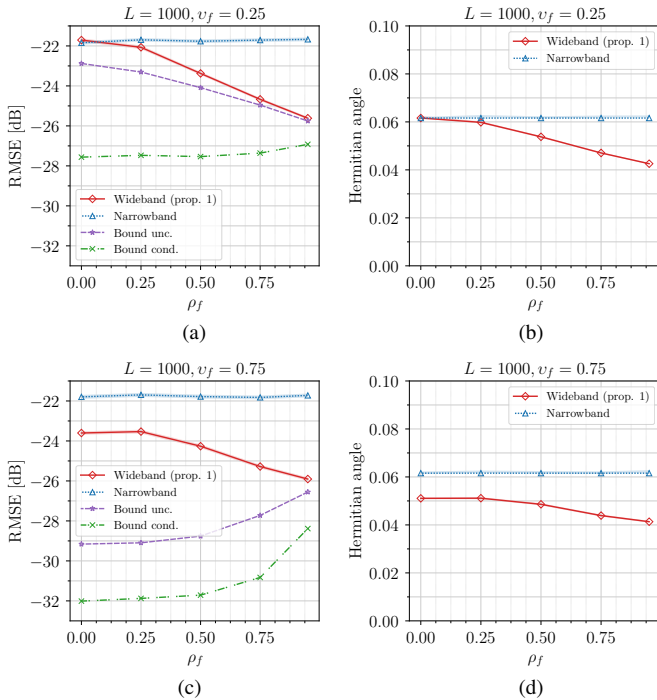


Fig. 3. Algorithm performance under varying target frequency correlation ρ_f , with different levels of noise correlation v_f . The top two plots (a) and (b) represent less correlated noise ($v_f = 0.25$), while the bottom row (c) and (d) show highly correlated noise ($v_f = 0.75$). The left column corresponds to RMSE, and the right column shows the Hermitian angle.

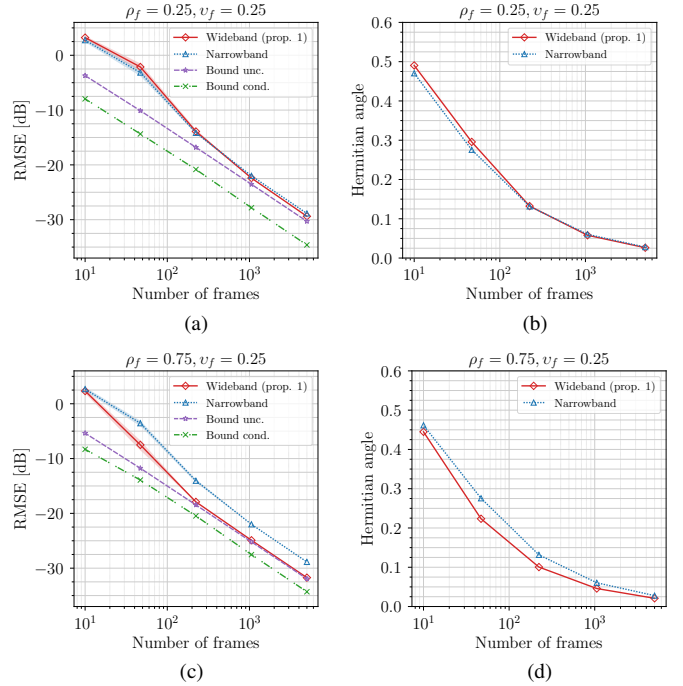


Fig. 4. Algorithm performance under varying number of time frames L , with different levels of target correlation ρ_f . The top two plots (a) and (b) represent a less correlated target ($\rho_f = 0.25$), while the bottom row (c) and (d) show a highly correlated target ($\rho_f = 0.75$). The left column corresponds to RMSE, and the right column shows the Hermitian angle.

from previous studies [40]. This seeming discrepancy can be better understood through analogy: when two point sources are located close together in space, they show maximal *spatial* correlation and exhibit similar correlation patterns, making it difficult to separate them. In our experiment, the noise and target sources have high *spectral* correlation, and they share the same correlation pattern (Equations (32) and (33)). We might say that they are “spectrally superimposed” because their powers and correlation coefficients are the same, yielding very similar spectral covariance matrices. As a result, they are harder to distinguish than two spectrally independent sources.

Varying number of frames L : We now analyze the performance of the algorithms when the number of frames L to estimate the target covariance matrix \mathbf{R}_d is varied between $L = 10$ and $L = 5000$ (Figure 4). As expected, both algorithms perform better when more frames are available. For low values of target and noise correlation (Figures 4a and 4b), the two algorithms perform similarly when the number of available time frames is large, whereas the proposed algorithm is slightly less accurate when L is small. When the target correlation is high, the wideband method shows smaller errors for any number of frames $L > 10$ and converges to the unconditional CRB for a high number of frames.

Varying SNR: This experiment analyzes the performance of the algorithms when the SNR varies between -10 and 20 dB (Figure 5). Unsurprisingly, both algorithms perform better when the noise is less prominent. The methods perform similarly for low target correlation values (Figures 5a and 5b). In contrast, for high target correlation (Figures 5c and 5d), the proposed method shows significant performance gains of up to 8 dB in RMSE and 0.05 rad in Hermitian angle in noisy scenarios. Both algorithms are close to the unconditional CRB for high

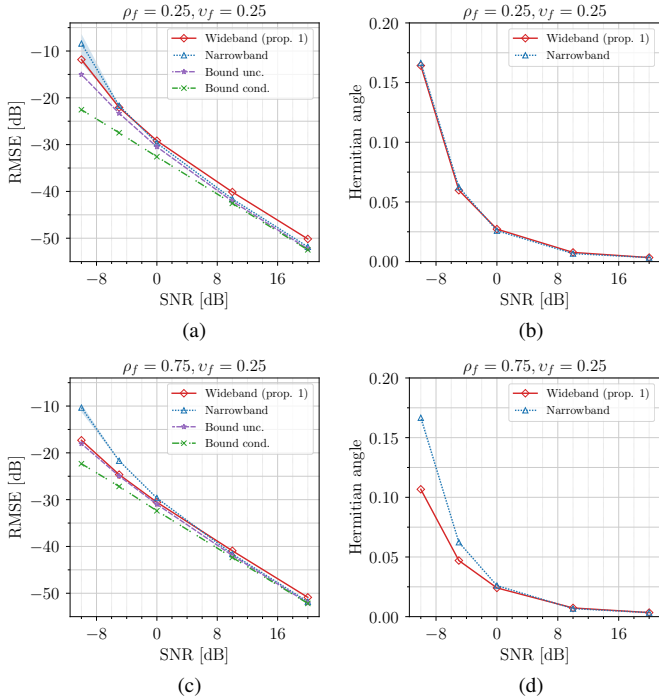


Fig. 5. Algorithm performance under varying SNR, with different levels of target correlation ρ_f . The top two plots (a) and (b) represent a less correlated target ($\rho_f = 0.25$), while the bottom row (c) and (d) show a highly correlated target ($\rho_f = 0.75$). The left column corresponds to RMSE, and the right column shows the Hermitian angle.

SNR values.

B. Equicorrelated, different powers

In the second set of experiments, we extend the ‘equicorrelated’ scenario described in Section VI-A, by incorporating varying signal powers across different frequency components and sensors. This scenario is not only more realistic than the previous one, but it also leads to more diverse spectral correlation patterns — that is, covariance matrices — for the target and the noise signal, limiting the “spectral superposition” phenomenon observed in Section VI-A. In this simulation model, special care must be taken to ensure the validity of the simulated covariance matrices \mathbf{R}_v and \mathbf{R}_s .

Let $[v]_{km} = v_{km}$ be the noise signal at frequency k and sensor m , with variance $\mathbb{E}[|v_{km}|^2] = V_{km}^2$. By the Cauchy–Schwarz inequality, it is known that the covariance between the two discrete complex random variables $v_{k_1 m_1}, v_{k_2 m_2}$, corresponding to the $(k_1 m_1, k_2 m_2)$ element of \mathbf{R}_v , is upper-bounded by:

$$|\mathbb{E}[v_{k_1 m_1} v_{k_2 m_2}^*]|^2 \leq \mathbb{E}[|v_{k_1 m_1}|^2] \mathbb{E}[|v_{k_2 m_2}|^2]. \quad (34)$$

Therefore, we can simulate \mathbf{R}_v with a two-step procedure. First, the variances V_{km}^2 on the diagonal of \mathbf{R}_v are drawn from a uniform distribution $\mathcal{U}(\epsilon, 0.5)$, where $\epsilon > 0$ is a small positive number.

Next, the covariance values are calculated as

$$\mathbb{E}[v_{k_1 m_1} v_{k_2 m_2}^*] = \begin{cases} 0, & \text{if } m_1 \neq m_2, \\ v_f \sqrt{V_{k_1 m_1}^2 V_{k_2 m_2}^2} & \text{if } m_1 = m_2, \end{cases} \quad (35)$$

where the factor $v_f \in [0, 1]$ models the noise inter-frequency correlation. Because $v_f \leq 1$, Equation (35) leads to covariance

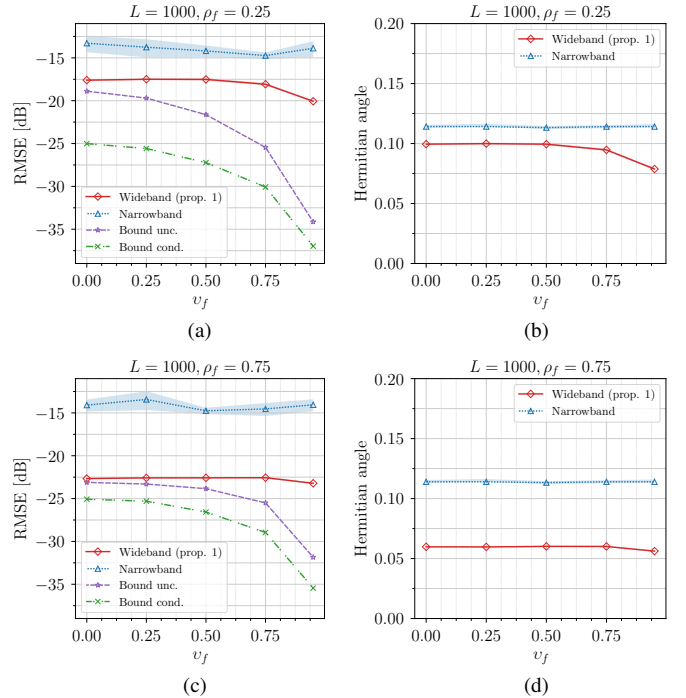


Fig. 6. Algorithm performance for non-uniform target and noise powers under varying noise frequency correlation v_f , with different levels of target correlation ρ_f . The top two plots (a) and (b) represent a less correlated target ($\rho_f = 0.25$), while the bottom row (c) and (d) show a highly correlated target ($\rho_f = 0.75$). The left column corresponds to RMSE, and the right column shows the Hermitian angle.

values that are always smaller than their theoretical maxima. The correlations across different sensors are set to 0 since we model spatially uncorrelated noise. Finally, \mathbf{R}_v is rescaled by a global noise variance V^2 to yield the desired SNR according to Equation (31). Analogously, the desired covariance matrix at the source is given by:

$$[\mathbf{R}_s]_{k_1 k_2} = \begin{cases} \sigma_{k_1 k_2}^2 \sim \mathcal{U}(\epsilon, 0.5) & \text{if } k_1 = k_2, \\ \rho_f \sqrt{\sigma_{k_1 k_1}^2 \sigma_{k_2 k_2}^2} & \text{if } k_1 \neq k_2. \end{cases} \quad (36)$$

The desired covariance matrix at the receivers follows again from Equations (6) and (7). The sampling procedure and the other simulation parameters follow from Section VI-A.

Varying noise correlation v_f : The performance of the algorithms is examined as the noise frequency correlation v_f varies from 0 to 1 (Figure 6). The wideband algorithm outperforms the narrowband one in all cases. The difference in accuracy is larger when the target correlation ρ_f is higher (Figures 6c and 6d), reaching an improvement of up to 8 dB RMSE and 0.05 rad. Notice that the performance gains are more significant than in the ‘equal powers’ scenario of Section VI-A. We also observe that the error of the SVD-direct algorithm slightly decreases for very high noise correlation $v_f \geq 0.75$. Still, the gap between the unconditional CRB and the algorithms indicates that further improvements are possible. Moreover, the wideband method shows more stable predictions with a narrower confidence interval for RMSE compared to the narrowband approach. We attribute the reduced variance of the wideband method to the averaging effect of the SVD across frequency components (see Algorithm 1).

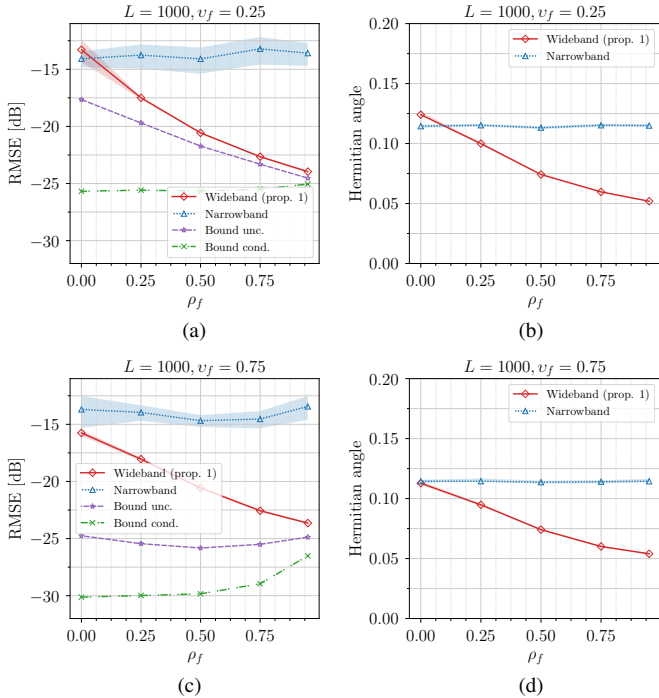


Fig. 7. Algorithm performance for non-uniform target and noise powers, under varying target frequency correlation ρ_f , with different levels of noise correlation v_f . The top row ((a) and (b)) represents less correlated noise ($v_f = 0.25$), while the bottom row ((c) and (d)) shows highly correlated noise ($v_f = 0.75$). The left column corresponds to RMSE, and the right column shows the Hermitian angle.

Varying target correlation ρ_f : Next, we turn to one of the key experiments of the present study, where we analyze the performance of the algorithms as the target frequency correlation ρ_f varies between 0 and 1 for arbitrary noise and signal powers (Figure 7). The wideband algorithm takes advantage of higher target spectral correlations ρ_f , as already observed in Section VI-A: both for low and high noise correlation, SVD-direct has significantly better performance for higher values of ρ_f , reaching improvements of 10 dB RMSE and 0.05 rad Hermitian angle. On the other hand, CW performs slightly better when the target correlation is completely absent ($\rho_f = 0$). A likely explanation is that the narrowband approach exploits the a priori knowledge that the target signal is uncorrelated across frequency. However, we argue that the scenario where $\rho_f = 0$ is unlikely to occur in practice for the reasons highlighted in Section I. Turning our focus to the performance bounds, we notice that the SVD-direct method achieves the CRB if a high target correlation is present, meaning that further improvements in accuracy in this scenario are not possible.

Varying number of frames L : We now evaluate the different approaches when estimating the covariance matrices with varying numbers of time frames L (Figure 8). The narrowband and wideband approaches exhibit similar performance for scenarios with low target and noise correlation (Figures 8a and 8b). The benchmark method is slightly more accurate when only a few frames are available ($L < 50$), whereas the proposed algorithm outperforms CW for a higher number of frames. Because wideband spectral-spatial covariance matrices are considerably larger than narrowband spatial covariance matrices, accurate estimation of the former requires more realizations. When the

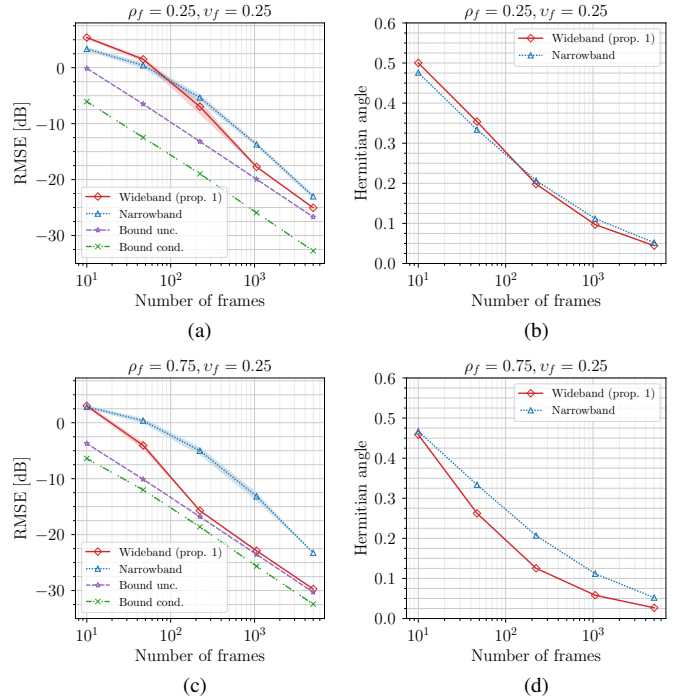


Fig. 8. Algorithm performance for non-uniform target and noise powers, under varying number of time frames L , with different levels of target correlation ρ_f . The top row ((a) and (b)) represents less correlated target ($\rho_f = 0.25$), while the bottom row ((c) and (d)) shows highly correlated target ($\rho_f = 0.75$). The left column corresponds to RMSE, and the right column shows the Hermitian angle.

target is highly correlated (Figures 8c and 8d), the wideband method consistently matches or outperforms the narrowband method.

Varying SNR: Lastly, in Figure 9, we examine the performance for various SNR levels. For low target and noise spectral correlation (Figures 9a and 9b), the two algorithms perform comparably, with the wideband method being marginally less accurate for higher SNRs. By contrast, when the target correlation is high, as in Figures 9c and 9d, the two approaches perform similarly for less noisy scenarios, but the wideband method has a considerably lower error for lower SNRs, with a reduction of up to 11 dB RMSE and 0.12 rad Hermitian angle at -10 dB SNR.

C. Real data simulations

The third set of experiments tests the algorithms on real speech data. The target signal consists of an anechoic female speech recording from the Harvard Word List⁵. We include a recorded washing machine sound from the ESC-50 database [41] to introduce noise. The target and the noise signals are convolved with the RIRs from the database in [42]. The impulse responses are recorded in a room with a size of $6 \times 6 \times 2.4$ m. Their average reverberation time is $RT_{60} = 0.36$ s. The linear microphone array has 8 sensors with 8 cm inter-distance. Before convolution, the target RIR is cut so that its length equals the length of a single STFT frame. To simulate challenging realistic conditions, the target and interferer sources are placed 1 m away from the microphones, at angles of 75° and 60° , respectively. Therefore, the target and interfering

⁵“Speech Intelligibility CD” from Neil Thompson Shade

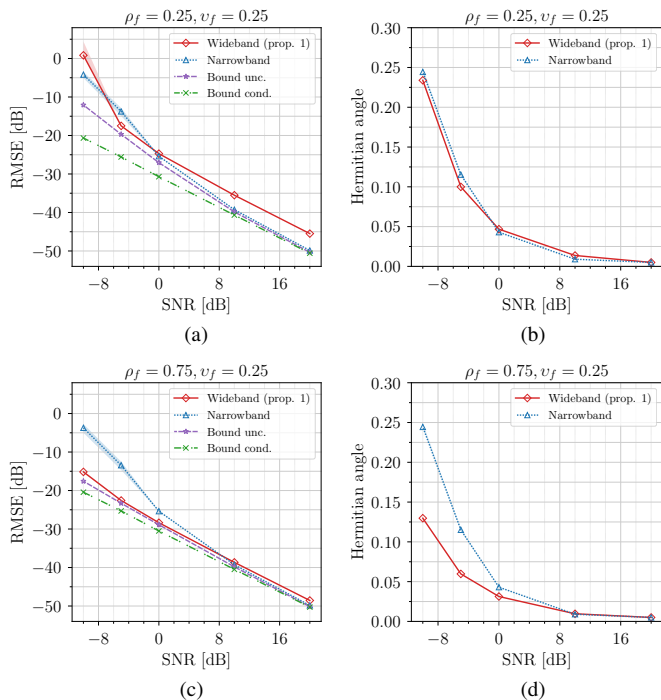


Fig. 9. Algorithm performance for non-uniform target and noise powers under varying SNR, with different levels of target correlation ρ_f . The top row ((a) and (b)) represents less correlated target ($\rho_f = 0.25$), while the bottom row ((c) and (d)) shows highly correlated target ($\rho_f = 0.75$). The left column corresponds to RMSE, and the right column shows the Hermitian angle.

sources are spatially close to each other but exhibit different spectral properties. In each of the 50 Monte Carlo iterations, segments of length 0.38 s, equivalent to $L = 5$ non-overlapping time frames, are randomly selected for both the target and noise signals. Silent samples are discarded. The default SNR for the interferer is set to 0 dB. We use the first $M = 4$ microphones where not differently specified. The sampling rate is set to 16 kHz. The STFT analysis is performed with window length $K_2 = 1024$ corresponding to $K = (K_2/2) + 1 = 513$ bins for the positive frequencies, and a 75% overlap, utilizing a square-root Hann window function, such that the block-shift equals $R = 256$ samples. To focus the analysis on relevant frequency bands and limit computational complexity, we only consider frequency components between 0.08 kHz to 4.0 kHz. When calculating the errors on the RTF estimates, we only retain the frequency bands for which the average power of the target signal at the microphones is no more than 35 dB lower than that of the loudest frequency band.

The noise covariance matrix $\hat{\mathbf{R}}_v$ is estimated from a separate realization of the noise-only signal whose duration is 2 s. A distinct noise realization is used for each Monte Carlo iteration. The covariance matrices $\hat{\mathbf{R}}_x$ and $\hat{\mathbf{R}}_v$ are estimated from phase-adjusted STFT data, as described in Equation (11), to account for the phase shifts caused by overlapping frames. To gauge the improvements brought by the phase-corrected covariance estimator, we also depict the accuracy of the wideband and narrowband algorithms when utilizing the classical sample covariance estimator (Equation (9)). Errors based on the sample covariance estimate with the original phase values are indicated by appending “orig-phase” to the RTF estimator name.

The wideband and narrowband algorithms, both with and without phase correction, are assessed based on the Hermitian

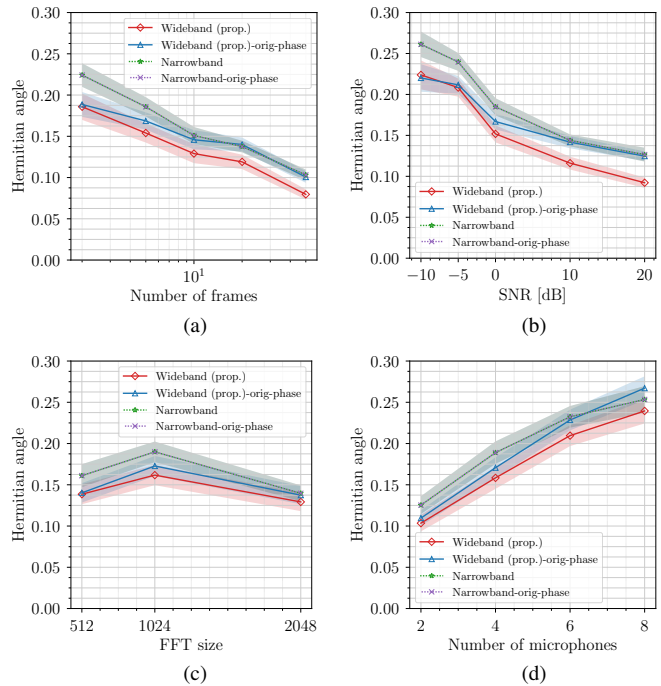


Fig. 10. Performance of the algorithms for real speech data, under (a) varying number of time frames L , (b) varying SNR, (c) varying FFT size, and (d) varying number of microphones. The error metric is the Hermitian angle.

angle metric across different conditions. These conditions include variations in the number of time frames (Figure 10a), the SNR (Figure 10b), the STFT size K_2 (Figure 10c), and the number of microphones M (Figure 10d). The proposed phase-adjusted wideband algorithm outperforms the narrowband benchmark in all four experiments of Figure 10. The performance gap between wideband and narrowband algorithms remains largely unchanged under varying conditions. As anticipated, the phase correction does not affect the performance of the narrowband algorithm, which does not rely on inter-frequency correlations (cf. Section III-A). On the other hand, the wideband algorithm benefits significantly from incorporating phase-adjusted covariance matrices, especially in scenarios with a higher number of available time frames (L) or microphones (M), or when the SNR is high. The impact of phase correction appears to diminish under conditions where the covariance estimates are compromised due to a low number of time frames or a low SNR.

VII. ADDITIONAL DISCUSSION

Our experiments yielded valuable insights into the performance of the narrowband CW and the wideband SVD-direct methods for RTF estimation, comparing them with the conditional and the unconditional performance bounds. Let us now examine the key findings.

Our investigation reveals a consistent trend favoring the wideband approach in scenarios with higher target correlation. Unlike the narrowband method, which remains unaffected by varying noise spectral correlation, the wideband approach also demonstrates occasional performance improvements when dealing with highly correlated noises.

The CRB analysis reveals a fascinating insight: when the noise spectral correlation v_f is high, significant potential exists

for further improvements in wideband channel estimation. While this discovery pertains to channel estimation, it points to potential applications across various parameter estimation tasks. The finding also provides a theoretical foundation for the observed empirical evidence in certain parametric and machine-learning approaches. Notably, some DNNs that operate on the entire time-frequency representation outperform narrowband alternatives in various speech enhancement tasks [25], [28]. It also offers a partial explanation for the intelligibility gains experienced by humans when detecting speech affected by harmonic noises [17].

The real-speech experiments confirm that natural speech possesses spectral correlations that can be exploited by the SVD-direct algorithm, leading to improved RTF estimation performance in all the scenarios under analysis. However, it is worth noting that the wideband algorithm may not surpass narrowband algorithms in certain settings, such as when dealing with highly non-stationary noise sources. This limitation arises from the inherent challenge of estimating large spectral-spatial covariance matrices from a limited number of frames. For instance, typical speech has about 10-20 different sounds per second [43, Chapter 15.3]. This dynamic nature makes the estimation of spectral patterns more demanding compared to spatial patterns, which depend on the positions of the speaker and the listener. Improved spectral correlation estimates may result by modeling the signals under analysis as realizations of cyclostationary processes, a particular class of spectrally correlated processes [44].

VIII. CONCLUSION

The uncorrelation of frequency components of a signal is a ubiquitous assumption that is often not verified in practice due to STFT processing and the non-stationary nature of signals. In this paper, we investigated the role of spectral correlations in spatial processing and proposed a new subspace-based algorithm for the channel estimation task. Indeed, accurate knowledge of the acoustic transfer functions between target speakers and microphones is crucial for spatial filtering in applications like MVDR beamforming.

Extensive numerical experiments demonstrated the superior performance of our wideband approach over the maximum-likelihood narrowband benchmark, yielding gains of more than 10 dB RMSE in scenarios involving spectral correlations and low SNR. The proposed SVD-direct algorithm also exhibited competitive performance with real reverberant speech data contaminated by directional interferers and spatially uncorrelated noise. These achievements are obtained without compromising conceptual interpretability, as the channel estimate can be computed in closed form with just a few lines of code.

Furthermore, we derived CRBs for wideband channel estimation, revealing the potential for substantial accuracy improvements when noise, and to a lesser extent, the target exhibits high-frequency correlation. This study serves as a starting point for understanding the impact of spectral correlations on parameter estimation for array processing. Future endeavors will focus on refining the estimation of spectral-spatial covariance matrices, conducting more comprehensive tests on real-world measurements, and analyzing the influence

of spectral correlation in speech enhancement and acoustic source separation.

APPENDIX A

PROOF OF CONDITIONAL CRB [EQUATION (26)]

Proof. To obtain the Cramér–Rao bound for the unknown parameters θ , we first calculate the derivatives of the log-likelihood function with respect to the unknown parameters to form the Fisher information matrix. Notice that the log-likelihood is a real-valued function of a complex variable θ . Thus, by evaluating the gradients using Wirtinger derivatives [35], we can make use of the following properties.

Lemma 2 *Let $f : \mathbb{C}^p \times \mathbb{C}^p \times \mathbb{C}^q \times \mathbb{C}^q \mapsto \mathbb{R}$ be a real scalar function of four complex variables $w, w^* \in \mathbb{C}^p$ and $z, z^* \in \mathbb{C}^q$. Then*

- (a) $\nabla_z f = (\nabla_{z^*} f)^*$.
- (b) $\nabla_z \nabla_w^H f = (\nabla_{z^*} \nabla_{w^*}^H f)^*$.

Proof.

- (a) Follows from the fact the gradient operators are complex conjugates while f is real.
- (b) $\nabla_z \nabla_w^H f = \nabla_z \nabla_{w^*}^T f = (\nabla_{w^*} \nabla_z^T)^T f = (\nabla_{w^*} \nabla_{z^*}^H)^T f = (\nabla_{z^*} \nabla_{w^*}^H f)^*$. \square

For notational convenience, we define $\mathcal{L}(\theta) = \ln p(\mathbf{X}; \theta)$. We will begin by evaluating the bottom-right quadrant of the Fisher information matrix (Equation (21)), defined as $-\mathbb{E}[\nabla_{a^*} \nabla_{a^*}^H \mathcal{L}(\theta)]$. Expanding the matrix product, the partial derivative of the log-likelihood $\mathcal{L}(\theta)$ in Equation (25) with respect to a_k^* is given by

$$\nabla_{a_k^*} \mathcal{L}(\theta) = -\nabla_{a_k^*} \left(\sum_{l=1}^L (\mathbf{y}(l) - \mathbf{A} \mathbf{s}(l))^H \mathbf{R}_v^{-1} \mathbf{v}(l) \right) \quad (37)$$

$$= \nabla_{a_k^*} \left(\sum_{l=1}^L \sum_{j=1}^{KM} s_j^*(l) \mathbf{a}_j^H \mathbf{R}_v^{-1} \mathbf{v}(l) \right) \quad (38)$$

$$= \sum_{l=1}^L s_k^*(l) \mathbf{e}_k^T \mathbf{R}_v^{-1} \mathbf{v}(l). \quad (39)$$

The second order derivative evaluates to

$$\nabla_{a_k^*} \nabla_{a_m} \mathcal{L}(\theta) = -\sum_{l=1}^L s_k^*(l) \mathbf{e}_k^T \mathbf{R}_v^{-1} \mathbf{e}_m s_m(l). \quad (40)$$

This leads to

$$-\mathbb{E}[\nabla_{a^*} \nabla_{a^*}^H \mathcal{L}(\theta)] = \sum_{l=1}^L \mathbf{S}(l)^H \mathbf{R}_v^{-1} \mathbf{S}(l), \quad (41)$$

where we defined

$\mathbf{S}(l) = \text{diag}(s(l))$. With this, the Fisher information matrix is given by (cf. Lemma 2) $\mathbf{I}_\theta = \text{blkdiag}(\mathbf{B}^*, \mathbf{B})$, where $\text{blkdiag}(\cdot)$ is the operator that constructs a block diagonal matrix from the given matrices, and

$\mathbf{B} = \sum_{l=1}^L \mathbf{S}(l)^H \mathbf{R}_v^{-1} \mathbf{S}(l)$. The block-diagonal matrix \mathbf{I}_θ can be inverted block-wise, leading to

$$\mathbf{I}_\theta^{-1} = \text{blkdiag}((\mathbf{B}^*)^{-1}, \mathbf{B}^{-1}). \quad (42)$$

The variance of unbiased estimators of the ATF is, therefore, bounded by $\text{var}(\hat{a}_i) \geq [(B^*)^{-1}]_{ii}$, $i = 1, \dots, M$.

Transfer functions can be estimated in relation to a reference sensor r with a function $\mathbf{g}(\cdot)$ defined in Equation (23). Choosing $r = 1$ as a reference sensor, the Jacobian matrix can be written as

$$\nabla_{\theta} \mathbf{g} = [\nabla_{\mathbf{a}} \mathbf{g} \quad \nabla_{\mathbf{a}^*} \mathbf{g}] = [\nabla_{\mathbf{a}} \mathbf{g} \quad \mathbf{0}_{KM \times KM}], \quad (43)$$

where the right block of the gradient, $\nabla_{\mathbf{a}^*} \mathbf{g}$, is null because $\mathbf{g}(\cdot)$ does not depend on \mathbf{a}^* . We can further partition the left block of the gradient in K “fat” matrices $\nabla_{\mathbf{a}} \mathbf{g} = [\nabla_{\mathbf{a}_1}^T \mathbf{g}, \dots, \nabla_{\mathbf{a}_K}^T \mathbf{g}]^T$, where $\nabla_{\mathbf{a}_k} \mathbf{g} \in \mathbb{C}^{M \times KM}$, $k = 1, \dots, K$. Individual blocks $\nabla_{\mathbf{a}_k} \mathbf{g}$ can be written as

$$\begin{bmatrix} \mathbf{0}_{M \times (k-1)M} & \begin{bmatrix} 0 & 0 & 0 & \dots & 0 \\ -a_{k2} a_{k1}^{-2} & a_{k1}^{-1} & 0 & \dots & 0 \\ -a_{k3} a_{k1}^{-2} & 0 & a_{k1}^{-1} & \dots & 0 \\ \vdots & \vdots & \vdots & \ddots & \vdots \\ -a_{kM} a_{k1}^{-2} & 0 & \dots & 0 & a_{k1}^{-1} \end{bmatrix} & \mathbf{0}_{M \times (K-k)M} \end{bmatrix}, \quad (44)$$

so that $\nabla_{\mathbf{a}} \mathbf{g}$ shows a block-diagonal structure. With this, we have from Equation (42) and Equation (22)

$$\mathbf{R}_{\hat{\gamma}} \succeq (\nabla_{\theta} \mathbf{g}) \mathbf{I}_{\theta}^{-1} (\nabla_{\theta}^H \mathbf{g}) = (\nabla_{\mathbf{a}} \mathbf{g}) (\mathbf{B}^*)^{-1} (\nabla_{\mathbf{a}}^H \mathbf{g}). \quad (45)$$

The CRB corresponds to the diagonal elements of the matrix at the right-hand side of Equation (45), as stated in Equation (26). \square

APPENDIX B

PROOF OF UNCONDITIONAL CRB [EQUATION (28)]

We first list some derivative rules (e.g., [37]) for a generic square matrix $\mathbf{X}(\theta)$, where the values of \mathbf{X} depend on θ .

$$\nabla_{\theta_i} \ln(\mathbf{X}) = \text{tr}(\mathbf{X}^{-1} \nabla_{\theta_i} \mathbf{X}), \quad (46)$$

$$\nabla_{\theta_i} \text{tr}(\mathbf{X}) = \text{tr}(\nabla_{\theta_i} \mathbf{X}), \quad (47)$$

$$\nabla_{\theta_i} \mathbf{X}^{-1} = -\mathbf{X}^{-1} (\nabla_{\theta_i} \mathbf{X}) \mathbf{X}^{-1}. \quad (48)$$

The computation of the unconditional CRB requires the calculation of first- and second-order derivatives of the log-likelihood in Equation (27), reproduced here for easy reference:

$$\mathcal{L}(\theta) = -L \ln |\pi \mathbf{R}_x| - L \text{tr}(\hat{\mathbf{R}}_x \mathbf{R}_x^{-1}). \quad (49)$$

Proof. The partial derivative of the log-likelihood $\mathcal{L}(\theta)$ in Equation (27) with respect to a_k^* is given by

$$\nabla_{a_k^*} \mathcal{L}(\theta) = -L \text{tr}(\mathbf{R}_x^{-1} \mathbf{F}_k) - L \text{tr}(\mathbf{R}_x^{-1} \mathbf{F}_k \mathbf{R}_x^{-1} \hat{\mathbf{R}}_x), \quad (50)$$

where we introduced $\mathbf{F}_k = \nabla_{a_k^*} \mathbf{R}_x = \mathbf{A} \mathbf{R}_s \mathbf{E}^{kk}$ and \mathbf{E}^{ij} is zero everywhere and 1 at entry ij . The first term on the right-hand side of Equation (50) is obtained directly from Equation (46). The second term is obtained by using the derivative of the trace and of the matrix inverse as given by Equation (47) and Equation (48), respectively, along with the cyclic property of the trace operator. It is important to note that the estimate $\hat{\mathbf{R}}_x$ is independent of the parameter vector \mathbf{a} . The second-order partial derivative of $\mathcal{L}(\theta)$ writes

$$\begin{aligned} \nabla_{a_k^*} \nabla_{a_k^*} \mathcal{L}(\theta) = \\ -L \nabla_{a_m} [\text{tr}(\mathbf{R}_x^{-1} \mathbf{F}_k) + \text{tr}(\mathbf{R}_x^{-1} \mathbf{F}_k \mathbf{R}_x^{-1} \hat{\mathbf{R}}_x)]. \end{aligned} \quad (51)$$

The derivatives of the two terms can be evaluated separately. For the first term in Equation (51), we have

$$\begin{aligned} \nabla_{a_m} \text{tr}(\mathbf{R}_x^{-1} \mathbf{F}_k) &= \text{tr}(\nabla_{a_m} \mathbf{R}_x^{-1} \mathbf{F}_k) = \\ &= \text{tr}(-\mathbf{R}_x^{-1} \mathbf{G}_m \mathbf{R}_x^{-1} \mathbf{F}_k + \mathbf{R}_x^{-1} \mathbf{H}_{mk}), \end{aligned} \quad (52)$$

which is obtained by applying the product rule together with Equation (47) and Equation (48). Here, \mathbf{G}_m and \mathbf{H}_{mk} are defined as

$$\mathbf{G}_m = \nabla_{a_m} \mathbf{R}_x = \mathbf{E}^{mm} \mathbf{R}_s \mathbf{A}^H, \quad (53)$$

$$\mathbf{H}_{mk} = \nabla_{a_m} \mathbf{F}_k = \nabla_{a_m} \nabla_{a_k^*} \mathbf{R}_x = \mathbf{E}^{mm} \mathbf{R}_s \mathbf{E}^{kk}. \quad (54)$$

The second term in Equation (51) is given by

$$\begin{aligned} \nabla_{a_m} \text{tr}(\mathbf{R}_x^{-1} \mathbf{F}_k \mathbf{R}_x^{-1} \hat{\mathbf{R}}_x) &= \text{tr} \nabla_{a_m} (\mathbf{R}_x^{-1} \hat{\mathbf{R}}_x \mathbf{R}_x^{-1} \mathbf{F}_k) = \\ \text{tr} \left[\mathbf{R}_x^{-1} \hat{\mathbf{R}}_x \mathbf{R}_x^{-1} (\mathbf{G}_m \mathbf{R}_x^{-1} \mathbf{F}_k - \mathbf{H}_{mk} + \mathbf{F}_k \mathbf{R}_x^{-1} \mathbf{G}_m) \right], \end{aligned} \quad (55)$$

which was again obtained by utilizing the product rule, Equation (47), Equation (48), and rearranging the resulting terms. By combining Equation (52) and Equation (55), the negative expected second-order partial derivative follows as

$$\begin{aligned} -\mathbb{E}[\nabla_{a_m} \nabla_{a_k^*} \mathcal{L}(\theta)] &= \\ &= -\mathbb{E} \left(L \text{tr} [-\mathbf{R}_x^{-1} (\mathbf{G}_m \mathbf{R}_x^{-1} \mathbf{F}_k - \mathbf{H}_{mk})] + \right. \\ &+ L \text{tr} \left[\mathbf{R}_x^{-1} \hat{\mathbf{R}}_x \mathbf{R}_x^{-1} (\mathbf{G}_m \mathbf{R}_x^{-1} \mathbf{F}_k - \mathbf{H}_{mk} + \mathbf{F}_k \mathbf{R}_x^{-1} \mathbf{G}_m) \right] \left. \right) \\ &= -L \text{tr} (\mathbf{R}_x^{-1} \mathbf{F}_k \mathbf{R}_x^{-1} \mathbf{G}_m). \end{aligned} \quad (56)$$

To collect the expected values of the second-order partial derivative, we define a matrix \mathbf{C}_1 such that $[\mathbf{C}_1]_{mk} = -\mathbb{E}[\nabla_{a_m} \nabla_{a_k^*} \mathcal{L}(\theta)]$. The elements of the bottom left block of the Fisher information matrix can be similarly obtained as $[\mathbf{C}_2]_{mk} = -\mathbb{E}[\nabla_{a_m} \nabla_{a_k} \mathcal{L}(\theta)] = L \text{tr}(\mathbf{R}_x^{-1} \mathbf{G}_k \mathbf{R}_x^{-1} \mathbf{G}_m)$, and the elements $-\mathbb{E}[\nabla_{a_m}^* \nabla_{a_k^*} \mathcal{L}(\theta)]$ of the top right block follow as \mathbf{C}_2^H from Lemma 2. The inverse of the Fisher information matrix for the unconditional case can then be represented by:

$$\mathbf{I}_{\theta}^{-1} = \begin{bmatrix} \mathbf{C}_1^* & \mathbf{C}_2^H \\ \mathbf{C}_2 & \mathbf{C}_1 \end{bmatrix}^{-1} = \begin{bmatrix} \mathbf{C} & * \\ * & * \end{bmatrix}, \quad (57)$$

where $\mathbf{C} \in \mathbb{C}^{KM \times KM}$ is obtained by selecting the first KM rows and columns from \mathbf{I}_{θ}^{-1} . To derive the bound for estimating the relative transfer function, we employ the mapping $\mathbf{g}(\cdot)$ as defined in Equation (23). Using Equation (22), the inverse Fisher information matrix is left- and right-multiplied by $\nabla_{\theta} \mathbf{g}$, which is defined in Equation (43), resulting in the final form of the bound given by Equation (28). \square

REFERENCES

- [1] S. Gannot, E. Vincent, S. Markovich-Golan, and A. Ozerov, “A Consolidated Perspective on Multimicrophone Speech Enhancement and Source Separation,” *IEEE/ACM Transactions on Audio, Speech, and Language Processing*, vol. 25, no. 4, pp. 692–730, Apr. 2017.
- [2] E. Hadad, S. Doclo, and S. Gannot, “The Binaural LCMV Beamformer and its Performance Analysis,” *IEEE/ACM Transactions on Audio, Speech, and Language Processing*, vol. 24, no. 3, pp. 543–558, Mar. 2016.
- [3] S. Gannot, D. Burshtein, and E. Weinstein, “Signal enhancement using beamforming and nonstationarity with applications to speech,” *IEEE Transactions on Signal Processing*, vol. 49, no. 8, pp. 1614–1626, Aug. 2001.

- [4] S. Doclo, S. Gannot, M. Moonen, and A. Spriet, "Acoustic Beamforming for Hearing Aid Applications," in *Handbook on Array Processing and Sensor Networks*. John Wiley & Sons, Ltd, 2010, pp. 269–302.
- [5] I. Cohen, "Relative transfer function identification using speech signals," *IEEE Transactions on Speech and Audio Processing*, vol. 12, no. 5, pp. 451–459, Sep. 2004.
- [6] R. Varzandeh, M. Taseska, and E. A. P. Habets, "An iterative multichannel subspace-based covariance subtraction method for relative transfer function estimation," in *2017 Hands-free Speech Communications and Microphone Arrays (HSCMA)*, Mar. 2017, pp. 11–15.
- [7] A. I. Koutrouvelis, R. C. Hendriks, R. Heusdens, and J. Jensen, "Robust Joint Estimation of Multimicrophone Signal Model Parameters," *IEEE/ACM Transactions on Audio, Speech, and Language Processing*, vol. 27, no. 7, pp. 1136–1150, Jul. 2019.
- [8] P. Hoang, Z.-H. Tan, J. M. de Haan, and J. Jensen, "Joint Maximum Likelihood Estimation of Power Spectral Densities and Relative Acoustic Transfer Functions for Acoustic Beamforming," in *ICASSP 2021 - 2021 IEEE International Conference on Acoustics, Speech and Signal Processing (ICASSP)*, Jun. 2021, pp. 6119–6123.
- [9] C. Li, J. Martinez, and R. C. Hendriks, "Low Complex Accurate Multi-Source RTF Estimation," in *ICASSP 2022 - 2022 IEEE International Conference on Acoustics, Speech and Signal Processing (ICASSP)*, May 2022, pp. 4953–4957.
- [10] C. Li and R. C. Hendriks, "Noise PSD Insensitive RTF Estimation in a Reverberant and Noisy Environment," in *ICASSP 2023 - 2023 IEEE International Conference on Acoustics, Speech and Signal Processing (ICASSP)*, Jun. 2023, pp. 1–5.
- [11] C. Li, J. Martinez, and R. C. Hendriks, "Joint Maximum Likelihood Estimation of Microphone Array Parameters for a Reverberant Single Source Scenario," *IEEE/ACM Transactions on Audio, Speech, and Language Processing*, vol. 31, pp. 695–705, 2023, conference Name: IEEE/ACM Transactions on Audio, Speech, and Language Processing.
- [12] A. Napolitano, "A - Nonstationary signal analysis," in *Cyclostationary Processes and Time Series*, A. Napolitano, Ed. Academic Press, Jan. 2020, pp. 471–478. [Online]. Available: <https://www.sciencedirect.com/science/article/pii/B9780081027080000285>
- [13] G. Giannakis, "Cyclostationary Signal Analysis," in *Digital Signal Processing Fundamentals*. CRC Press, Nov. 2009, vol. 20094251, pp. 1–32.
- [14] Y. Liu, Z. Tan, H. Hu, L. J. Cimini, and G. Y. Li, "Channel Estimation for OFDM," *IEEE Communications Surveys & Tutorials*, vol. 16, no. 4, pp. 1891–1908, 2014.
- [15] J. Wolfe, M. Garnier, N. H. Bernardoni, and J. Smith, "The Mechanics and Acoustics of the Singing Voice: Registers, Resonances and the Source-Filter Interaction," in *The Routledge Companion to Interdisciplinary Studies in Singing, Volume I: Development*. Routledge, 2020.
- [16] B. Dong, "Characterizing resonant component in speech: A different view of tracking fundamental frequency," *Mechanical Systems and Signal Processing*, vol. 88, pp. 318–333, May 2017.
- [17] H. Gockel, B. C. J. Moore, and R. D. Patterson, "Asymmetry of masking between complex tones and noise: The role of temporal structure and peripheral compression," *The Journal of the Acoustical Society of America*, vol. 111, no. 6, pp. 2759–2770, Jun. 2002.
- [18] B. Moore, *An Introduction to the Psychology of Hearing*. Emerald, 2012. [Online]. Available: <https://books.google.nl/books?id=LM9U8e28pLMC>
- [19] C. Trahiotis and R. M. Stern, "Lateralization of bands of noise: Effects of bandwidth and differences of interaural time and phase," *The Journal of the Acoustical Society of America*, vol. 86, no. 4, pp. 1285–1293, Oct. 1989, publisher: Acoustical Society of America. [Online]. Available: <http://asa.scitation.org/doi/10.1121/1.398743>
- [20] I. A. McCowan, "Robust speech recognition using microphone arrays," Ph.D. dissertation, Queensland University of Technology, 2001.
- [21] J. Dmochowski, J. Benesty, and S. Affes, "On Spatial Aliasing in Microphone Arrays," *IEEE Transactions on Signal Processing*, vol. 57, no. 4, pp. 1383–1395, Apr. 2009. [Online]. Available: <http://ieeexplore.ieee.org/document/4696048/>
- [22] S. Markovich, S. Gannot, and I. Cohen, "Multichannel Eigenspace Beamforming in a Reverberant Noisy Environment With Multiple Interfering Speech Signals," *IEEE Transactions on Audio, Speech, and Language Processing*, vol. 17, no. 6, pp. 1071–1086, Aug. 2009.
- [23] S. Markovich-Golan and S. Gannot, "Performance analysis of the covariance subtraction method for relative transfer function estimation and comparison to the covariance whitening method," in *2015 IEEE International Conference on Acoustics, Speech and Signal Processing (ICASSP)*, Apr. 2015, pp. 544–548.
- [24] S. Markovich-Golan, S. Gannot, and W. Kellermann, "Performance analysis of the covariance-whitening and the covariance-subtraction methods for estimating the relative transfer function," in *2018 26th European Signal Processing Conference (EUSIPCO)*, Sep. 2018, pp. 2499–2503.
- [25] J. Benesty, J. Chen, and E. A. P. Habets, "The Bifrequency Spectrum in Speech Enhancement," in *Speech Enhancement in the STFT Domain*, ser. SpringerBriefs in Electrical and Computer Engineering, J. Benesty, J. Chen, and E. A. Habets, Eds. Berlin, Heidelberg: Springer, 2012, pp. 93–101.
- [26] H. Huang, L. Zhao, J. Chen, and J. Benesty, "A minimum variance distortionless response filter based on the bifrequency spectrum for single-channel noise reduction," *Digital Signal Processing*, vol. 33, pp. 169–179, Oct. 2014.
- [27] K. Tan, Z.-Q. Wang, and D. Wang, "Neural Spectrospatial Filtering," *IEEE/ACM Transactions on Audio, Speech, and Language Processing*, vol. 30, pp. 605–621, 2022.
- [28] K. Tesch and T. Gerkmann, "Insights Into Deep Non-linear Filters for Improved Multi-channel Speech Enhancement," *IEEE/ACM Transactions on Audio, Speech, and Language Processing*, vol. 31, pp. 563–575, 2023, arXiv:2206.13310 [cs, eess]. [Online]. Available: <http://arxiv.org/abs/2206.13310>
- [29] J. Antoni, G. Xin, and N. Hamzaoui, "Fast computation of the spectral correlation," *Mechanical Systems and Signal Processing*, vol. 92, pp. 248–277, Aug. 2017. [Online]. Available: <https://www.sciencedirect.com/science/article/pii/S0888327017300134>
- [30] G. H. Golub and C. F. Van Loan, *Matrix computations*, 4th ed., ser. Johns Hopkins studies in the mathematical sciences. Baltimore: The Johns Hopkins University Press, 2013, oCLC: ocn824733531.
- [31] S. Doclo and M. Moonen, "Robust Adaptive Time Delay Estimation for Speaker Localization in Noisy and Reverberant Acoustic Environments," *EURASIP Journal on Advances in Signal Processing*, vol. 2003, no. 11, p. 495250, Dec. 2003. [Online]. Available: <https://asp-erasipjournals.springeropen.com/articles/10.1155/S111086570330602X>
- [32] R. R. Nadakuditi and J. W. Silverstein, "Fundamental Limit of Sample Generalized Eigenvalue Based Detection of Signals in Noise Using Relatively Few Signal-Bearing and Noise-Only Samples," *IEEE Journal of Selected Topics in Signal Processing*, vol. 4, no. 3, pp. 468–480, Jun. 2010. [Online]. Available: <http://ieeexplore.ieee.org/document/5447639/>
- [33] E. Anderson, Z. Bai, C. Bischof, S. Blackford, J. Demmel, J. Dongarra, J. Du Croz, A. Greenbaum, S. Hammarling, A. McKenney, and D. Sorensen, *LAPACK Users' Guide*, 3rd ed. Philadelphia, PA: Society for Industrial and Applied Mathematics, 1999.
- [34] P. Stoica and A. Nehorai, "Performance study of conditional and unconditional direction-of-arrival estimation," *IEEE Transactions on Acoustics, Speech, and Signal Processing*, vol. 38, no. 10, pp. 1783–1795, Oct. 1990, conference Name: IEEE Transactions on Acoustics, Speech, and Signal Processing.
- [35] D. H. Brandwood, "A complex gradient operator and its application in adaptive array theory," *IEE Proceedings F (Communications, Radar and Signal Processing)*, vol. 130, no. 1, pp. 11–16, Feb. 1983, publisher: IET Digital Library. [Online]. Available: <https://digital-library.theiet.org/content/journals/10.1049/ip-f-1.1983.0003>
- [36] A. van den Bos, "A Cramer-Rao lower bound for complex parameters," *IEEE Transactions on Signal Processing*, vol. 42, no. 10, pp. 2859–, Oct. 1994, conference Name: IEEE Transactions on Signal Processing.
- [37] S. M. Kay, *Fundamentals of statistical signal processing: estimation theory*. USA: Prentice-Hall, Inc., 1993.
- [38] Peter J. Schreier and Louis L. Scharf, *Statistical Signal Processing of Complex-Valued Data: The Theory of Improper and Noncircular Signals*. Cambridge: Cambridge University Press, 2010.
- [39] D. G. Altman and J. M. Bland, "Standard deviations and standard errors," *BMJ : British Medical Journal*, vol. 331, no. 7521, p. 903, Oct. 2005.
- [40] H. Kasasbeh, R. Viswanathan, and L. Cao, "Noise Correlation Effect on Detection: Signals in Equicorrelated or Autoregressive(1) Gaussian," *IEEE signal processing letters*, vol. 24, no. 7, pp. 1078–1082, Jul. 2017.
- [41] K. J. Piczak, "ESC: Dataset for Environmental Sound Classification," in *Proceedings of the 23rd Annual ACM Conference on Multimedia*. ACM Press, 2015, pp. 1015–1018. [Online]. Available: <http://dl.acm.org/citation.cfm?doi=2733373.2806390>
- [42] E. Hadad, F. Heese, P. Vary, and S. Gannot, "Multichannel audio database in various acoustic environments," in *2014 14th International Workshop on Acoustic Signal Enhancement (IWAENC)*, 2014, pp. 313–317.
- [43] A. F. Molisch, *Wireless communications*, 2nd ed. Wiley : IEEE, 2011, OCLC: ocn613645390.
- [44] W. A. Gardner, A. Napolitano, and L. Paura, "Cyclostationarity: Half a century of research," *Signal Processing*, vol. 86, no. 4, pp. 639–697, 2006. [Online]. Available: <https://linkinghub.elsevier.com/retrieve/pii/S0165168405002409>